Research Square

Preprints are preliminary reports that have not undergone peer review.
They should not be considered conclusive, used to inform clinical practice,
or referenced by the media as validated information.

Fluorine-incorporated strain-released large ZnSe/ZnS:F quantum dots enabling high-efficiency and stable pure-blue light-emitting diodes

Wallace C.H. Choy

chchoy@eee.hku.hk

The University of Hong Kong https://orcid.org/0000-0002-9535-4076

Zhiwei Long

The University of Hong Kong

Jiayun Sun

The University of Hong Kong

Qi Xiong

The University of Hong Kong

Xiaoyong Mo

Department of Chemistry, HKU-CAS Joint Laboratory on New Materials, Faculty of Science, The University of Hong Kong, Hong Kong

Yulin Mao

University of Macau

Guichuan Xing

Joint Key Laboratory of the Ministry of Education, Institute of Applied Physics and Materials Engineering, University of Macau https://orcid.org/0000-0003-2769-8659

Article

Keywords:

Posted Date: July 15th, 2026

DOI: https://doi.org/10.21203/rs.3.rs-10116335/v1

License: This work is licensed under a Creative Commons Attribution 4.0 International License.
Read Full License

Additional Declarations: There is **NO** Competing Interest.

Abstract

Weakly-confined, large ZnSe quantum dots (QDs) are promising eco-friendly pure-blue emitters featuring narrow and symmetrical emission spectra. However, achieving high emission efficiency requires the epitaxial growth of a thick protective shell, fundamentally constrained by the extensive faceted surfaces and high elastic modulus of the large ZnSe core, leading to interfacial intermixing and strain-induced dislocation defects. Herein, we report a fluorine-incorporated strain-released strategy via dual-stage shell growth, including interface stabilization and strain relaxation, that enables the growth of defect-free, thick ZnS shells. Initially, high-reactivity zinc–sulfur precursors are employed to establish a well-defined core/shell interface that suppresses sulfur in-diffusion-associated spectral blue-shifts. Subsequently, the synergistic introduction of hydrofluoric acid and 2-ethylhexanoic acid drives the incorporation of fluoride ions into the interstitial sites of the ZnS lattice. The induced expansion of the host lattice dynamically relaxes accumulated misfit strain, permitting the coherent, defect-free growth of thick shells that extend well beyond their thermodynamic critical thickness. The resultant strain-released, thick-shelled ZnSe/ZnS:F QDs exhibit near-unity photoluminescence quantum yields and achieve strong amplified spontaneous emission. The fabricated QD-based light-emitting diodes, showing symmetric emission peaking at 451 nm with a linewidth of 20 nm, achieve an external quantum efficiency of 24.5% and a brightness of 17,140 cd m-², championing ZnSe QD-based devices.

Introduction

The construction of type-I core/shell (C/S) structures in colloidal semiconductor quantum dot (QD) systems has driven remarkable advancements in QD light-emitting diodes (QLEDs) applications, realizing external quantum efficiency (EQEs) over 20% and operational stability comparable to commercial organic LEDs[1-4]. Most of these achievements have involved toxic cadmium-based QDs, while the cadmium-free, eco-friendly blue-emitting QDs still face significant challenges in achieving comparable performances. For the wide bandgap ZnSe (2.7 eV for bulk) semiconductor material, notable progress has been made in achieving pure-blue emission (450–470 nm) through doping tellurium (Te) into small-sized ZnSe QDs[5-8]. However, the doping strategy inevitably leads to spectral asymmetry caused by localized enrichment of Te atoms within the alloyed systems[7,9]. Very recently, weakly-confined, large ZnSe QDs have demonstrated great potential for pure-blue emission, featuring narrow and symmetrical emission spectra, owing to their minimal bandgap variations[10-12]. Additionally, large QDs excel in suppressing Auger recombination and Joule heating generation, thereby enhancing electroluminescence stability and reducing efficiency roll-off in QLEDs[13-15]. Despite these, few studies on ZnSe QD-based QLEDs have realized high efficiency or high brightness. The best reported EQE and brightness are limited to 12.2% and 1223 cd m^{-2}, respectively, along with dissatisfactory operational lifetimes[10,16,17], which is far from their ternary ZnTeSe QDs counterparts. The main reason lies in the challenges of the coherent growth of thick passivation shell for ZnSe QDs.

ZnS is a widely adopted passivation shell material for various fluorescent QDs (e.g., CdSe, InP, ZnSe, and perovskite) due to its wide bandgap of ~3.7 eV, which facilitates forming type-I band alignment core/shell structures, thus enhancing their photoluminescence (PL) quantum yields (QY)[18-21]. Typically, a thick shell is required to improve the emission stability and environmental resilience under high operating voltage by preventing oxidation quenching[16,22,23]. Compared to small-sized ZnSe QDs, growing ZnS shell on weakly-confined large ZnSe QDs (over 8 nm) is considerably more challenging due to their increased surface area, prominent faceted features, and reduced compressibility[24-26]. In addition, Zn-based chalcogenides exhibit a very high elastic modulus, which leads to high strain energy and limits their tolerance to lattice misfit strain[27]. When the shell thickness surpasses a critical threshold, dislocation lattice defects are prone to form, leading to deformed morphologies and degraded optical properties[20,26]. In the ZnSe-based QD system, it was reported that the growth of ZnS shells often results in spectral blue-shifting, which becomes more pronounced as shell thickness increases[6,10,20,28]. Apparently, this blue-shifting effect limits the use of large ZnSe QDs for display applications to cover the requisite pure-blue range. The challenge of addressing strain-induced defect formation and unintended blue shifts remains a major bottleneck in the synthesis of high-quality pure-blue emitting ZnSe QDs.

In this study, we propose a strain-released shell growth strategy through interstitial fluorine-doping enabled by a dual-stage approach, including interface stabilization and strain relaxation to address the thermodynamic constraints of growing a defect-free thick ZnS shell on large ZnSe QDs (Fig. 1a). By separating the shell growth into distinct interface-stabilization and strain-relaxation stages, we effectively decouple the challenges of interfacial anion diffusion and lattice mismatch. The initial growth of a uniform ZnS buffer layer locks the core surface, preventing the blue-shifts caused by interfacial anion intermixing. In the second stage, interstitial fluorine doping, by deliberately introducing hydrofluoric acid (HF) and the branched entropic ligand 2-ethylhexanoic acid (EHA), expands the host ZnS lattice to accommodate the accumulated misfit strain, enabling the coherent growth of thick ZnS shells that extend well beyond the intrinsic critical thickness without introducing dislocation defects or photoluminescence quenching. The resultant strain-released ZnSe/ZnS:F QDs realize near-unity PL QYs, and superior optical stability. Additionally, the QD film exhibits strong amplified spontaneous emission (ASE) at 457 nm with a linewidth of 2.6 nm under pulsed excitation. QLEDs fabricated with these thick-shell QDs achieved an EQE of 24.5% and a brightness of 17,140 cd m^{-2}, with narrow and symmetrical electroluminescence (EL) spectra peaking at the pure-blue region, demonstrating great potential of large ZnSe QDs for pure-blue QLED display applications.

Synthesis of strain-released thick-shell C/S QDs

We synthesized monodisperse large ZnSe QDs with an average diameter of 8.6 nm (size distribution deviation <7%) via continuously injecting regulated Zn and Se precursors into the ZnSe seed reaction[12]. The transmission electron microscopy (TEM) characterizations of the obtained ZnSe seed and large ZnSe core QDs are shown in Fig. S1a-b. For the epitaxial growth kinetics of ZnS shell, low-reactivity zinc precursors (e.g., zinc stearate, zinc oleate) are preferred to produce uniform shell morphologies and

enhance optical properties through a slow, thermodynamically controlled growth[6,20,28]. We firstly adopted zinc oleate ($Zn(OA)_2$) and 1-octanethiol (OT) as shell precursors to initiate the growth of ZnS shell. The PL peak of the obtained ZnSe/ZnS (C/S) QDs shifts from 450 to 442 nm as the ZnS shell thickness increases to 8 monolayers (MLs) (Fig. 1b), the TEM image of the resultant C/S QDs is shown in Fig. S1c. This spectral blue-shift is mainly attributed to the formation of an intermixed core/shell interface due to sulfur in-diffusion to the ZnSe core[29,30] (Fig. S1d), which leads to an enlarged bandgap of the emissive core. Additionally, we observed that a thick ZnS shell could not uniformly grow onto such large ZnSe cores, with some unpassivated region due to a certain number of unreactive sites on the surface of large ZnSe QD (Fig. S1e, f).

To stabilize the core/shell interface and suppress the unintended spectral blue-shifts associated with shell coating, we propose a strain-released shell growth strategy through a dual-stage approach by employing high-reactivity zinc amine Zn(OLA) as shell precursor and introducing HF and EHA as additives during the secondary shell growth stage. The use of Zn(OLA) enables a well-defined core/shell interface, which inevitably results in a tensioned shell because the lattice constant of ZnS (a=5.41 Å) is smaller than ZnSe (a=5.67 Å). As a result, the resultant strained ZnSe/ZnS (s-C/S) QDs showcase red-shift with the increase of shell thickness, which is attributed to a transformation toward a quasi-type II band alignment, caused by strain-induced band offset[24,31]. However, the further growth of the ZnS shell would lead to broadening of the emission linewidth and degraded PL emission when the shell thickness exceeding 3 MLs (Fig. S1g), due to the formation of strain-induced lattice defects[25,32].

Hence, during the secondary shell growth stage (start with a critical shell thickness), we deliberately introduce both HF and EHA into the s-C/S(3ML) QD reactor to mitigate strain-induced defect formation, obtaining strain-released ZnSe/ZnS:F (sr-C/S) QDs that attain a near 100% PL QY and show a slight blue-shift during the strain-release process (Fig. 1c). To trace the precise role of each additive during shell growth, we systematically evaluated three distinct control series (Fig. 1d). In the first control series, omitting both HF and EHA additives, conventional undoped shell growth triggers severe strain accumulation, leading to catastrophic PL QY quenching as shell beyond a critical thickness of 3 MLs. In the second control series, implementing the HF etchant solely moderately increases the maximum PL QY from 61% to 83% via surface oxidative defects etching[4,6], and extends the critical thickness to 4 MLs. However, it fails to stave off structural collapse and PL degradation upon further shell thickness expansion (Fig. 1d). In addition, we observed that the solely or excessively use of HF would lead to the formation of by-product ZnF_2 nanoparticles (Fig. S2). Only under the concurrent action of HF and EHA does the system bypass these thermodynamic shell growth limits, maintaining near-unity PL QY without quenching even with the shell thickness up to 8 MLs. The resultant thick-shelled sr-C/S(8ML) QDs demonstrate significantly improved PL stability compared with the thin-shell QDs under ambient conditions (Fig. 1e).

Fig. 1f presents the morphology evolution of the C/S QDs with shell growth during the initial core/shell interface stabilization and the secondary strain-released stages. Without the presence of HF and EHA,

the further growth of ZnS shell onto the as-formed uniform s-C/S(3ML) QDs would result in deformed morphologies as well as poor PL properties. In addition, the selected-area electron diffraction (SAED) rings of the s-C/S(6ML) QDs become enlarged and widened compared with those of s-C/S(3ML) QDs, indicating accumulated excess strain and dislocation defects. By simultaneously introducing HF and EHA, an obvious morphological transformation occurred during the subsequent shell growth process. Because HF can initialize the formation of Zn–F bonds to stabilize (100) facet of the QD, leading to a reduction of the (111) facet with shell growth, thus showing a facet-directed growth manner[33,34]. The resultant sr-C/S(4ML) and sr-C/S(8ML) QDs show well-defined morphologies with a narrow size distribution deviation of ~6% and superior dispersibility; and the energy dispersive spectrometer (EDS) elemental mappings of the sr-C/S(8ML) QDs demonstrate their distinct thick ZnS-shelled structures (Fig. S3). Furthermore, under electron beam irradiation for five minutes, the sr-C/S(8ML) QDs do not exhibit void formation (Fig. S4), demonstrating their relaxed internal strain and enhanced structural stability[35,36]. In contrast, the thin-shell s-C/S(3ML) and sr-C/S(4ML) QDs show a degradation. The above experimental results explicitly demonstrate that the continuous, defect-free propagation of the crystalline shell requires an internal structural intervention uniquely mediated by the fluorine component and entropic ligands.

F-incorporated strain release mechanism in ZnS shell

Due to the lattice mismatch between the core and shell materials, the as-formed core/shell heterojunction is subjected to interfacial misfit strain that dictates the morphological evolution of the outer shell. In the ZnSe/ZnS system, the core/shell interface undergoes high strain energy due to the large Young's moduli characteristic of Zn-based chalcogenides compared to others such as Cd-based equivalents (Table S1). Consequently, edge dislocations easily form when the shell exceeds a critical threshold, prompting a transition to incoherent and irregular island growth (Stranski–Krastanov mode[32,37]), as schematically depicted in Fig. 2a. Under the conventional shell growth mode, the resultant s-C/S(3ML) QDs maintain regular morphologies, while a certain proportion of the s-C/S(4ML) QDs show deformed morphologies with distorted lattice arrangement (Fig. S5a). This structural deterioration is clearly visible in the aberration-corrected scanning transmission electron microscopy (STEM) image and geometric phase analysis (GPA) strain map of the s-C/S QDs with thicker shell thickness (Fig. 2b), which reveal extensive stacking faults (SF) along the (111) planes, non-uniform strain distributions, and an incoherent twin boundary. In contrast, for the F-incorporated thick-shelled sr-C/S QDs, the ZnS shell lattice is coherent with the ZnSe core (Fig. 2c), accompanied by a lattice expansion in the shell layer, as evidenced by a larger d-spacing of 2.07 Å for the (220) facet compared to 2.01 Å in the strained s-C/S QD, and the GPA image indicates negligible residual strain in the QD. Interestingly, for sr-C/S(8ML) QDs, we captured high-resolution TEM images of more than 100 particles, all of which exhibited no signs of lattice distortion (Fig. S5b).

To trace the strain evolution of C/S QDs with shell thickness under the conventional and F-incorporated shell growth, we acquired the XRD patterns of the obtained C/S QDs with different shell thicknesses (Fig. S6). According to Bragg’s law[38], we calculated the strain of the inner ZnSe core, and the strain curves are

shown in Fig. 2d. Through the F-incorporated shell growth approach, the calculated strain of the inner ZnSe core is as small as only 0.6% as the shell thickness increases up to 8 MLs, while the conventional approach leading to a strain of over 2%. To further evidence that the strain relaxation with shell thickness increasing attributes to F-incorporation induced lattice intervention, we conducted more atomic-scale high-resolution TEM lattice characterizations and studies (Fig. 2e). In the strained s-C/S QD, the d-spacing of the (111) plane contracts to 0.321 nm, which is substantially smaller than the 0.332 nm d-spacing of the native ZnSe core, revealing massive tension lattice strain within the shell layer. Upon introducing the F-incorporated growth strategy, the sr-C/S QD displays a d-spacing of 0.331 nm for the (111) plane, nearly identical to the native core value (Fig. 2f). This lattice expansion makes the outer shell matrix well match the core lattice constant, yielding a completely coherent core/shell interface with negligible residual strain.

To confirm that this lattice expansion of ZnS shell is caused exclusively by internal lattice-interstitial fluorine incorporation, we analyzed the chemical coordination environment using X-ray photoelectron spectroscopy (XPS). As shown in Fig. 2g, the Zn $2p_{3/2}$ XPS spectrum of the sr-C/S QD uniquely splits into a wide, asymmetric doublet that convolutes into distinct Zn–S (1021.9 eV) and Zn–F (1022.6 eV) bond components, verifying direct chemical integration into the host matrix. This matches the F 1s spectrum profile (Fig. 2h), which exhibits an asymmetric peak composed of both surface-adsorbed and internal lattice-interstitial F ions[39], contrasting sharply with the narrow, symmetric singlet obtained from purely surface-adsorbed control samples (Fig. S7a,b). Another piece of evidence of this internal spatial distribution of F ions was established via mono-atomic Ar ion sputtering depth profiling on a double-shelled model system ZnSe/ZnS:F/ZnS QDs that were fabricated by epitaxially growing a thin ZnS shell onto the sr-C/S(8ML) QDs (Fig. S7c). Before Ar ion beam sputtering, no fluorine signal is detected at the outermost shell interface. However, upon layer-by-layer removal of the outer pure ZnS capping shell, a robust interstitial fluorine signal emerges precisely within the underlying ZnS:F matrix layer, accompanied by a synchronous shift of the Zn Auger LMM spectra to higher binding energies (Fig. 2i, j), indicating the success of F-doping into the ZnS shell to form the ZnS:F layer.

In this strain release shell growth approach, the entropic ligand EHA ($C_8H_{16}O_2$), containing a branched-chain structure and a terminal carboxyl group, plays a pivotal role in enabling the F ions incorporation into ZnS shell lattice and enhancing the dispersibility of large QDs. The carboxyl group enhances the solubility of the zinc precursor, consequently, reducing the availability of excess zinc precursor to avoid the formation of ZnF_2 by-product. As a result, the presence of EHA increases and homogenizes the F ion concentration in the reaction solution, facilitating F incorporation into the ZnS shell and promoting more controlled shell growth. In our study, when HF and EHA were introduced in the ZnSe core solution, the F ions would be doped into the ZnSe core, resulting in self-trapped exciton emission[40] (Fig. S7d). Supporting this, the Se 3d XPS spectrum of F-doped ZnSe QDs shifts to higher binding energy compared to ZnSe QDs (Fig. S7e). In contrast, the Se 3d XPS spectra of shell-doped QDs show negligible shifting regardless of shell thicknesses (Fig. S7f). These observations suggest that the preformed thin ZnS shell is essential to prevent F ions diffusion into the ZnSe core. Furthermore, a branched-chain structure of

EHA can increase the intramolecular entropy and minimize the enthalpy for destroying the chain–chain interactions, thus substantially enhancing the solubility of QDs in the reaction solution[41] (Fig. S8).

Optical properties of strain-released thick-shell QDs.

As structural strain is typically accompanied by the formation of sub-bandgap dislocation traps, the s-C/S QDs suffer from severe defect-related non-radiative recombination, dragging the PL QY down below 30% as the shell thickness approaches 8 MLs. In contrast, due to the efficient strain relaxation by F incorporation, the sr-C/S QDs maintain a near 100% PL QY across the shell growth profile, demonstrating that the mitigation of internal lattice tension well eliminates deep-level trap states. To evaluate how this fluorine-mediated strain-released thick ZnS shell governs the photophysical behavior of the heterostructures, we used density functional theory (DFT) to calculate the density of states (DOS) for ZnSe/ZnS heterojunction crystal cells with a thin ZnS layer and a thick ZnS:F shell layer, respectively. The calculated DOS results indicate that the strained thin-shell heterojunction has mid-gap surface trap states near the conduction band minimum (Fig. 3a). The surface trap states act as local energy minima that hinder or delay electron-hole recombination while increasing the electron-transfer probability, resulting in reduced luminous efficiency[42]. For the ZnSe/ZnS:F heterojunction, the trap states are eliminated. Additionally, the bandgap becomes evidently enlarged with a thick F-incorporated ZnS layer, which may help lift the electronic state degeneracy to enable directional light emission of the inner core[43]. Supporting this, the sr-C/S(8ML) QDs have a larger Stokes shift of 89.4 meV than the 77.1 meV of s-C/S(3ML) QDs, and show a minimized concentration quenching effect of fluorescence (Fig. S9a-c).

Time-resolved photoluminescence results indicate that thin-shell s-C/S(3ML) QD film shows a significantly slower PL lifetime compared to the QD solution state (Fig. 3b), along with a spectral red-shift of 4 nm (Fig. S9d), revealing severe nonradiative recombination channels and electronic coupling energy transfer in the highly-packed QDs[44]. In contrast, the PL lifetime of the thick-shell sr-C/S(8ML) QD film exhibits a slight decrease compared to the QD solution state, and the PL spectra without shifting (Fig. S9e), demonstrating a reduced probability of excited carrier traps[45]. Benefiting from the combination of near-unity quantum efficiency and minimized electronic coupling energy transfer, the sr-C/S(8ML) QD film demonstrate robust amplified spontaneous emission (ASE) in the pure-blue spectral regime at 457 nm with a full width at half maximum (FWHM) of 2.6 nm under femtosecond laser pulsing excitation (Fig. 3c), showing great potential for pure-blue laser applications.

Low-temperature PL measurements were conducted to obtain more insights into the passivation effect with thick-shell structures. The obtained temperature-dependent PL spectra of different shelled QDs are presented in Fig. 3d. The thin-shell s-C/S(3ML) QDs show a distinct trap state-related emission tail at 77 K, while the thin-shell sr-C/S(4ML) QDs demonstrate reduced trap state-related emission intensities at low temperatures. In contrast, the thick-shell sr-C/S(8ML) QDs, the trap-state emission is nearly eliminated, indicating an effective passivation of mid-gap surface trap states with increased ZnS shell thickness. These findings are in strong agreement with the results from DFT calculations. We further determined the exciton binding energy (E_b) of these QDs by fitting the integrated PL intensity against the

temperature using the Arrhenius equation (Fig. 3e). The sr-C/S(4ML) QDs exhibit an E_b of 87 meV, surpassing the 66 meV observed in s-C/S(3ML) QDs. Moreover, the thick-shell sr-C/S(8ML) QDs show an even larger E_b of 114 meV, significantly exceeding that of thinner shelled QDs. These results indicate that the thick strain-released ZnS:F shell effectively enhances electron confinement of the large ZnSe QDs.

Fig. 3f presents the two-dimensional maps of transient absorption spectra of the s-C/S QDs with shell thicknesses of 3 and 6 MLs under 350 nm photoexcitation. The temporal evolution of the relative change in transmitted light intensity (ΔT/T) of the s-C/S(3ML) QDs reveals the bleaching signals of $1S_e$–$1S_h$ and $1P_e$–$1P_h$ transition states located at 442 and 380 nm, respectively. The s-C/S(6ML) QDs with deformed morphologies show splitting bleaching peaks, revealing a defect-related energy transformation process. Differently, the bleaching peaks of the sr-C/S(4ML) QDs show a narrowing trend and a slight blue-shift, which becomes more obvious for the thick-shell sr-C/S(8ML) QDs (Fig. 3g), indicating the elimination of strain-induced band offsets. The carrier dynamics demonstrate a slower decay process for the thick-shell QDs, indicative of reduced defect trap states due to improved shell passivation (Fig. 3h). Additionally, the thick-shell QDs show significantly enhanced resistance against anti-solvent purification (Fig. S9f). These findings underscore the critical role of shell strain engineering, in developing well-passivated, thick-shelled QDs with superior optical performances.

QLEDs fabrication and performance

In addition to improving the optical properties, a thick ZnS shell is also considered to balance charge injection in ZnSe/ZnS QDs, since the electronic mobility of bulk ZnSe is higher than that of ZnS, owing to the higher electron scattering rate in ZnS[46]. The thick-shell QDs showed a slightly widened bandgap (2.76 eV) in comparison to the 2.73 eV of the thin-shell QDs (Fig. S10a). The ultraviolet photoelectron spectroscopy (UPS) results of sr-C/S QDs reveal that the valence band maximum of the thick-shell QDs is 0.24 eV higher than that of thin-shell QDs (Fig. S10b). These shifts of energy level promote the injection of holes from the hole transport layer to the QD layer. Moreover, the upshifted conduction band minimum in thick-shell QDs can inhibit excessive electron injection. We further fabricated hole-only (ITO/PEDOT:PSS/PF8Cz/QDs/MoO_3/Al) and electron-only devices (ITO/ZnMgO/QDs/ZnMgO/Al) to confirm the above conclusion. The current density–voltage characteristics of single-carrier devices show that the hole current substantially increased for the thick-shell QDs while the electron current decreased (Fig. S10c), indicating more balanced charge injection within the thick-shelled C/S QDs

We constructed typical bottom-emitting QLEDs with a structure of ITO/PEDOT:PSS/PF8Cz/QDs/ZnMgO/Al, as shown in Fig. 4a, including the energy levels for each layer, in which the QDs with varied shell thicknesses are employed. The SEM image of the spin-coating QD layer shows excellent smoothness (Fig. S11a), and the cross-sectional TEM image of the optimized QLED with sr-C/S(8ML) QDs indicates that the thickness of the QD layer is approximately 40 nm (Fig. S11b). The operating voltage-dependent electroluminescence (EL) spectra of the thick-shell QD-based QLED are presented in Fig. 4b. The spectra exhibit a symmetrical emission peak at 451 nm with a FWHM of 20 nm. Notably, the emission peak and linewidth remain unchanged with increasing biases to 8 V (Fig. S12a), whereas the

control QLEDs using the strained QDs exhibit obvious spectral red-shifts and broadening as the bias increases (Fig. S12b), which is attributed to the quantum-confined stark effect[47]. Due to the strain-induced dislocation lattice defects, the deformed thick-shell s-C/S(6ML) QDs produce poor charge injection and a low EQE of 2.6% (Fig. S12c,d). Transient EL dynamics analysis shows that the sr-C/S(8ML) QDs have a faster EL rise time compared to the s-C/S(3ML) QDs (Fig. 4c), indicating that the strain-released thick-shell structure of ZnSe QD promotes more efficient hole injection and recombination.

The current density–voltage–luminance characteristics of the QLEDs with different-shelled QDs in the emitting layer are presented in Fig. 4d. Compared with the devices using thin-shell QDs, the target QLEDs using the thick-shell QDs show lower leakage current at low biases (below the turn-on voltage of ~2.5 V). The maximum brightness achieved is 17,140 cd m^{-2} for the sr-C/S(8ML) QD-based device, and 5,534 cd m^{-2} for the sr-C/S(4ML) QD-based device. Whereas the brightness of the control QLEDs with s-C/S(3ML) QDs reaches only 1,320 cd m^{-2}. Significantly, the maximum EQE for the target devices with sr-C/S(8ML) QDs reaches 24.5% (Fig. 4e), which is nearly five-fold higher than the 5.1% of the s-C/S(3ML) QD-based devices. We further evaluated the operational stability of the devices under constant current density. The thick-shell sr-C/S(8ML) QD-based QLEDs exhibit a significantly enhanced half-lifetime (T_{50}) of 30.1 hours at an initial luminance exceeding 1,000 cd m^{-2}, which is more than 20 times longer than the 1.5 hours recorded for the thin-shell s-C/S(3ML) QD-based QLEDs (Fig. 4f). The histograms of the peak EQEs from over 35 devices for each type of QDs are presented in Fig. 4g, demonstrating their high reproducibility. To our best knowledge, the brightness of the strain-released thick-shell sr-C/S(8ML) QD-based devices represents a great breakthrough among ZnSe-based QLEDs (Fig. 4h). The EQE values reported in this work are some of the highest levels for blue QLEDs covering the state-of-the-art cadmium-based QLEDs (Fig. 4i, Table S2).

Methods

Chemicals and reagents

Zinc acetate ($Zn(OAc)_2$, 99.99%), selenium (Se, 99.99%, powder), 1-octanethiol (OT, 99%), oleic acid (OA, 90%), oleylamine (OLA, 90%), trioctylphosphine (TOP, 90%), 1-octadecene (ODE, 90%), tetramethylammonium hydroxide (TMAH, 97%), 2-ethylhexanoic acid (EHA, 99.9%), and liquid paraffin (90%) were purchased from Aladdin. Diphenylphosphine (DPP, 99%), hydrofluoric acid (HF, 48 wt%), and hexane (extra dry, >99%) were purchased from Energy-Chemical. Acetone (extra dry, >99%), ethanol (EtOH, extra dry, >99%), chlorobenzene (extra dry, 99.8%), octane (extra dry, >99%), ethyl acetate (extra dry, >99%), dimethyl sulfoxide (DMSO,99.7%), zinc acetate dihydrate ($Zn(OAc)_2{\cdot}2H_2O$, 99.99%), and magnesium acetate tetrahydrate ($Mg(OAc)_2{\cdot}4H_2O$, 99.98%) were purchased from Sigma-Aldrich. PEDOT:PSS (Al 4083) was ordered from H.C. Starck GmbH, Germany. PF8Cz was purchased from Xi'an Polymer Light Technology. All reagents were used as received without further experimental purification.

Preparation of Se-X (X=DPP, ODE)

[0.4M] Se-DPP precursor: 0.8 mmol Se powders (0.8 mmol) mixed with DPP (2 ml) in N_2-filled glove box, then heated to 80 °C until the powders were completely dissolved. The solution was then cooled to room temperature and stored in the glove box for subsequent use. [0.4M] Se-ODE precursor: A mixture of Se powders (8 mmol) and ODE solvent (20 ml) was vacuumed at 120 °C for 40 min. It was then heated to 220 °C under N_2 and kept for 1 hour, next heated to 240 °C and kept for 1 hour until the powders were completely dissolved. Then the solution was cooled down to 80 °C for further use.

Preparation of Zn-Se and Zn-S precursor solutions

Zn-Se precursor for epitaxial growth: $Zn(OAc)_2$ (8 mmol), OA (10 mmol), and OLA (10 mmol) were mixed with ODE (15 ml) solvent in a 100-ml three-neck flask by stirring and the mixture was heated to 120 °C under vacuum and kept it at that temperature for 1 hour, then the solution was heated to 160 °C for 20 min under N_2 atmosphere until the solution became clear. Next, the solution was cooled to 80 °C and mixed with Se-ODE (10 ml) and kept it at room temperature for further use. Zn-S precursor: $Zn(OAc)_2$ (8 mmol), OLA (8 mmol) were mixed with ODE (15 ml) solvent in a three-neck flask by stirring and the mixture was heated to 120 °C under vacuum and kept at that temperature for 1 hour to obtain the Zn(OLA) precursor. Then, the solution was cooled down to 80°C and mixed with OT (10 mmol) to obtain Zn-S precursor. After that, the solution was kept at room temperature for further use.

Synthesis of ZnSe seeds and large ZnSe cores

$Zn(OAc)_2$ (0.5 mmol), OA (0.5 mmol), and OLA (3 mmol) were mixed with liquid paraffin (15 ml) solvent in a 100-ml three-neck flask by stirring and the mixture was heated to 120 °C under vacuum and kept at that temperature for 1 hour. The atmosphere was changed to N_2, and then the solution was heated to 300 °C, followed by rapidly injecting 0.5 ml Se-DPP (0.2 mmol) and reacting for 40 min to produce ZnSe seeds with an average size of 4 nm. At the same temperature, the Zn-Se precursor solution (10 ml) was continuously injected (0.6 ml min^{-1}) into the ZnSe seeds reactor by an injection pump, followed by maintaining for 30 min to fabricate large ZnSe cores.

Synthesis of strained C/S QDs and strain-released C/S QDs

The above crude ZnSe core solution was cooled to 120 °C and evacuated for 30 min to remove the reaction by-product $H_2O(g)$. After that, the atmosphere was changed to N_2 and then the solution was heated to 290 °C. Then, the Zn-S precursor solution (4 ml) was continuously injected (0.5–0.7 ml min^{-1}) into the ZnSe core solution through an injection pump to obtain strained thin-shell ZnSe/ZnS QDs. An additional injection of 6 ml of Zn-S precursor in the solution would form the strained thick-shell QDs. To obtain strain-released ZnSe/ZnS QDs, diluted HF in acetone (0.1 ml, 10 wt%) was dropwise added (using a plastic syringe) into the strained thin-shell QDs solution at 290 °C. The solution was maintained for reacting 10 min, followed by injecting EHA (0.1 ml), then the Zn-S precursor solution (3 ml) was

continuously injected (0.6 ml min^{-1}) to synthesize the strain-released thin-shell QDs with shell thickness of 4 MLs. After four rounds of the above shell growth procedure, the strain-released thick-shell QDs with shell thickness of 8 MLs were finally obtained.

Purification of QDs

The above crude QD solution was cooled down to 50 °C, then an equal volume of hexane was injected with stirring. The solution was mixed with excess ethanol (with a volume ratio of 1:2) and centrifuged at 6,000 rpm for 3 min in a N_2-filled glove box. After three times of purification, the obtained QD precipitates were vacuumed for 5 min to obtain QD powders. The dried QD powders were re-dispersed in octane for further characterization and film fabrication.

Synthesis of ZnMgO nanoparticles

For a typical synthesis, $Zn(OAc)_2{\cdot}2H_2O$ (4.5 mmol) and $Mg(OAc)_2{\cdot}4H_2O$ (0.5 mmol) were mixed with dimethyl sulfoxide (30 ml) in a 100-ml three-neck flask by stirring at 60 °C for 20 min, and cooled down to room temperature (20 °C). Then, tetramethylammonium hydroxide (8 mmol) dissolved in ethanol solution (10 ml) was added dropwise to the above solution with vigorous stirring. Then the mixture was stirred for 12 hours under ambient conditions in a dry glovebox (humidity below 10%). The ZnMgO nanoparticles were purified three times with 120 ml of ethyl acetate and centrifuged at 6,000 rpm for 5 min. Finally, the ZnMgO nanoparticles were re-dispersed in ethanol and stored in a refrigerator.

Device fabrication

Patterned indium tin oxide (ITO) glass substrates with a sheet resistance of approximately 15 Ω sq^{-1} were cleaned consecutively with detergent, deionized water, acetone and ethanol in an ultrasonic bath, and then treated with ozone plasma for 40 min. PEDOT: PSS (Al 4083) solution was spin-coated onto ITO substrates at 3,500 rpm for 35 s, followed by baking at 150 °C for 10 min in air. Then, the coated substrates were transferred into a N_2-filled glove box for spin-coating PF8Cz, QDs and ZnMgO nanoparticle layers. The PF8Cz solution (8 mg ml^{-1} in chlorobenzene) was spin-coated at 2,000 rpm for 45 s, and baked at 150 °C for 20 min. The QD solution (20 mg ml^{-1}) was spin-coated at 2,500 rpm for 35 s and baked at 85 °C for 10 min. The ZnMgO nanoparticles solution (20 mg ml^{-1}) was spin-coated at 2,500 rpm for 35 s and baked at 75 °C for 10 min. Finally, an Al cathode (100 nm) was deposited by thermal evaporation in a high-vacuum chamber ($<5\times10^{-6}$ Pa).

Materials Characterization

Transmission electron microscopy (TEM), high-angle annular dark-field (HAADF) scanning transmission electron microscopy (STEM) and energy dispersive spectroscopy (EDS) measurements for QDs were performed on Thermo Scientific Talos F200X operated at 200 kV. Aberration-corrected transmission electron microscopy measurements were performed on a JEOL ARM 200F operated at 200 kV. SEM images were acquired using a Hitachi S-4800 field emission scanning electron microscope. A BRUKER

D8 advance X-ray diffractometer equipped with a Cu Kα radiation source (λ=1.54178 Å, maximum power, 40 kV, 40 mA) was used to record the X-ray diffraction (XRD) patterns. X-ray photoelectron spectroscopy (XPS) and ultraviolet photoelectron spectroscopy (UPS) were conducted using an ESCALAB QXi XPS Microprobe. The broadband femtosecond transient absorption (TA) measurements were performed by using the Ultrafast System HELIOS TA spectrometer. The laser source is the Coherent Astrella-1K-F Ultrafast Ti: Sapphire Amplifier (<100 fs, 1 kHz). The system is responsible for characterizing the carrier kinetics within 7 ns with a resolution below 100 fs. The 350 nm pump laser is generated by passing the fundamental frequency 800 nm femtosecond laser through an optical parametric amplifier (OPA). The broadband probe pulses were generated by focusing a small portion (around 2.5 μJ cm^{-2}) of the fundamental 800 nm laser pulses into a 2 mm sapphire plate. Steady-state PL spectra, PL QYs and TR-PL were measured by a PicoQuant FluoTime 300 spectrometer, and a laser diode with a peak wavelength of 375 nm was used as the excitation source. The temperature-dependent PL spectra were measured through a liquid nitrogen cryostat (OXFORD INSTRUMENTS OptistatDN2) equipped with a Mercury iTC temperature controller. Steady-state ultraviolet–visible (UV-vis) absorption spectra were measured by using the UV-2600 240V EN spectrophotometer. Dynamic light-scattering (DLS) spectra of QDs in octane solution were measured by a Zetasizer Ultra system. FTIR spectra were measured by FT/IR-6600 spectrometer (JASCO Inc.)

DFT calculation

Density functional theory (DFT) calculations were performed by using the CP2K package[48], hybrid Gaussian and plane wave density functional scheme and the Quickstep module[49], the Perdew-Burke-Ernzerhof (PBE) exchange correlation function[50], Goedecker-Teter-Hutter (GTH) pseudopotential[51], DZVP-MOLOPT-SR-GTH/TZVP-MOLOPT-SR-GTH/TZVP-MOLOPT-GTH basis sets were used to describe the system[49]. A plane-wave energy cut-off and relative cut-off of 400 Ry and 55 Ry have been employed, respectively. The energy convergence criterion was set to 10^{-6} Hartree. The DFT-D3(BJ) level correction for dispersion interactions was applied[52]. Structural optimization was performed using the Limited Memory Broyden-Fletcher-Goldfarb-Shannon (LBFGS) optimizer, until the maximum force was below 0.00045 Ry/Bohr (0.011 eV/Å).

Declarations

Data availability

The authors declare that the data supporting the findings of this study are available within the article and its Supplementary Information.

Acknowledgements

We acknowledge financial support from the project of the University Grant Council of the University of Hong Kong (grant No. 2302101786, and 2402101935), NSFC-RGC Collaborative Research Fund and

General Research Fund from the Research Grants Council of Hong Kong Special Administrative Region, China (grant No. CRS_HKU703/25, 17200823, 17310624 and 17304925). Innovation and Technology Fund from Innovation and Technology Commission of Hong Kong Special Administrative Region, China. (GHP/245/22SZ). Z.L. would like to acknowledge Dr. Huang Y. for assistance with the DFT calculations. Z.L. acknowledge Dr. Tan Y.Z. for the help of pump intensity-dependent PL test. Z.L. acknowledge Mr. Chan Y. F. Frankie, Dr. Zheng F. Y. Karen, and Dr. Mo X. Y. Wing from the Electron Microscopy Unit of the University of Hong Kong for providing material characterizations. We acknowledge Professor David Srolovitz for providing insightful comments on this work.

Author contributions

Z.L. and W.C.H.C. conceived the idea. W.C.H.C. coordinated and supervised the work. Z.L. performed most of the synthesis and characterization of the QDs. J.S. carried out the PL and TR-EL tests. Q.X. contributed to the TR-PL and DLS experiments. Y.M. and G.X. contributed to the TA test and analysis. X.M. contributed to the XPS depth profiling test and analysis. Z.L., and J.S. fabricated and characterized the QLED devices. Z.L. wrote the original draft, and W.C.H.C. revised and edited the draft. All authors discussed the results and commented on the paper.

Competing interests

The authors declare no competing interests.

References

1. Schlamp, M., Peng, X. & Alivisatos, A.-l. Improved efficiencies in light emitting diodes made with CdSe (CdS) core/shell type nanocrystals and a semiconducting polymer. *J. Appl. Phys.* **82**, 5837–5842 (1997).
2. Dai, X. *et al.* Solution-processed, high-performance light-emitting diodes based on quantum dots. *Nature* **515**, 96 –99 (2014).
3. Shen, H. *et al.* Visible quantum dot light-emitting diodes with simultaneous high brightness and efficiency. *Nat. Photon.* **13**, 192–197 (2019).
4. Won, Y.-H. *et al.* Highly efficient and stable InP/ZnSe/ZnS quantum dot light-emitting diodes. *Nature* **575**, 634–638 (2019).
5. Jang, E.-P. *et al.* Synthesis of alloyed ZnSeTe quantum dots as bright, color-pure blue emitters. *ACS Appl. Mater. Interfaces* **11**, 46062–46069 (2019).
6. Kim, T. *et al.* Efficient and stable blue quantum dot light-emitting diode. *Nature* **586**, 385–389 (2020).
7. Wu, Q. *et al.* Homogeneous ZnSeTeS quantum dots for efficient and stable pure-blue LEDs. *Nature* **639**, 633–638 (2025).
8. Shen, W.-S. *et al.* Dipole-assisted functionalization enables long-range ordering of ZnTeSe quantum dots for efficient and stable deep-blue electroluminescence. *Nat. Photonics* **20**, 571–578 (2026).

9. Han, C.-Y. *et al.* More than 9% efficient ZnSeTe quantum dot-based blue electroluminescent devices. *ACS Energy Lett.* **5**, 1568–1576 (2020).
10. Gao, M. *et al.* Bulk-like ZnSe Quantum Dots Enabling Efficient Ultranarrow Blue Light-Emitting Diodes. *Nano Lett.* **21**, 7252–7260 (2021).
11. Yang, Z. *et al.* A seed-mediated and double shell strategy to realize large-size ZnSe/ZnS/ZnS quantum dots for high color purity blue light-emitting diodes. *Nanoscale* **13**, 4562–4568 (2021).
12. Long, Z. *et al.* A reactivity-controlled epitaxial growth strategy for synthesizing large nanocrystals. *Nat. Synth.* **2**, 296–304 (2023).
13. Lee, K.-H. *et al.* Over 40 cd/A efficient green quantum dot electroluminescent device comprising uniquely large-sized quantum dots. *ACS Nano* **8**, 4893–4901 (2014).
14. Liu, B.-C. *et al.* Tailored large-particle quantum dots with high color purity and excellent electroluminescent efficiency. *Sci. Bull.* **70**, 905–913 (2025).
15. Wang, F. *et al.* Highly Efficient Blue Light-Emitting Diodes with Low Efficiency Roll-Off Based on Large-Size and Gradient Alloy Quantum Dots. *Small Methods* **10**, 2500598 (2026).
16. He, J. *et al.* Overcoming side reaction effects in the colloidal synthesis of ZnSe/ZnS core/shell quantum dots with an etching strategy. *Nano Res.* **17**, 7020–7026 (2024).
17. Chen, L. *et al.* ZnSe/ZnS Core/Shell Quantum Dots with Narrow Emission Bands for QLED Displays. *ACS Appl. Opt. Mater* **3**, 1800–1809 (2025).
18. Dabbousi, B. O. *et al.* (CdSe) ZnS core–shell quantum dots: synthesis and characterization of a size series of highly luminescent nanocrystallites. *J. Phys. Chem. B* **101**, 9463–9475 (1997).
19. Zhang, W. *et al.* InP/ZnS/ZnS core/shell blue quantum dots for efficient light-emitting diodes. *Adv. Funct. Mater.* **30**, 2005303 (2020).
20. Ji, B., Koley, S., Slobodkin, I., Remennik, S. & Banin, U. ZnSe/ZnS core/shell quantum dots with superior optical properties through thermodynamic shell growth. *Nano Lett.* **20**, 2387–2395 (2020).
21. Teku, J. A., Taylor, D. A. & Lee, J.-S. Thick ZnS Shells on $CsPbBr_3$ Quantum Dots by Colloidal-Atomic Layer Deposition for Enhanced Photoluminescence and Stability. *JACS Au* **5**, 4036–4043 (2025).
22. Pal, B. N. *et al.* 'Giant'CdSe/CdS core/shell nanocrystal quantum dots as efficient electroluminescent materials: strong influence of shell thickness on light-emitting diode performance. *Nano Lett.* **12**, 331–336 (2012).
23. Bisschop, S., Geiregat, P., Aubert, T. & Hens, Z. The impact of core/shell sizes on the optical gain characteristics of CdSe/CdS quantum dots. *ACS Nano* **12**, 9011–9021 (2018).
24. Smith, A. M., Mohs, A. M. & Nie, S. Tuning the optical and electronic properties of colloidal nanocrystals by lattice strain. *Nat. Nanotechnol.* **4**, 56–63 (2009).
25. Ji, B. *et al.* Strain-controlled shell morphology on quantum rods. *Nat. Commun.* **10**, 2 (2019).
26. Long, Z. *et al.* The strain effects and interfacial defects of large ZnSe/ZnS core/shell nanocrystals. *Small* **20**, 2306602 (2024).

27. Khenata, R. *et al.* Elastic, electronic and optical properties of ZnS, ZnSe and ZnTe under pressure. *Comput. Mater. Sci.* **38**, 29–38 (2006).
28. Shen, H. *et al.* High-efficient deep-blue light-emitting diodes by using high quality $Zn_xCd_{1-x}S$/ZnS core/shell quantum dots. *Adv. Funct. Mater.* **24**, 2367–2373 (2014).
29. Beane, G. A., Gong, K. & Kelley, D. F. Auger and carrier trapping dynamics in core/shell quantum dots having sharp and alloyed interfaces. *Acs Nano* **10**, 3755–3765 (2016).
30. Berends, A. C. *et al.* Interplay between surface chemistry, precursor reactivity, and temperature determines outcome of ZnS shelling reactions on $CuInS_2$ nanocrystals. *Chem. Mater* **30**, 2400–2413 (2018).
31. Jing, L. *et al.* Insight into strain effects on band alignment shifts, carrier localization and recombination kinetics in CdTe/CdS core/shell quantum dots. *J. Am. Chem. Soc.* **137**, 2073–2084 (2015).
32. Gong, K. & Kelley, D. F. A predictive model of shell morphology in CdSe/CdS core/shell quantum dots. *J. Chem. Phys.* **141** (2014).
33. Ghosh, S. & Manna, L. The many “facets” of halide ions in the chemistry of colloidal inorganic nanocrystals. *Chem. Rev.* **118**, 7804–7864 (2018).
34. Lee, Y. J. *et al.* Crystallographic and Photophysical Analysis on Facet-Controlled Defect-Free Blue-Emitting Quantum Dots. *Adv. Mater.* **36**, 2311719 (2024).
35. Yin, Y. *et al.* Formation of hollow nanocrystals through the nanoscale Kirkendall effect. *Science* **304**, 711–714 (2004).
36. Tang, J. *et al.* Morphology Evolution of Gradient-Alloyed $Cd_xZn_{1-x}Se_yS_{1-y}$@ZnS Core–Shell Quantum Dots during Transmission Electron Microscopy Determination: A Route to Illustrate Strain Effects. *J. Phys. Chem. C* **122**, 4583–4588 (2018).
37. Jiang, Z.-J. & Kelley, D. F. Stranski–Krastanov shell growth in ZnTe/CdSe core/shell Nanocrystals. *J. Phys. Chem. C* **117**, 6826–6834 (2013).
38. Pope, C. G. X-ray diffraction and the Bragg equation. *J. Chem. Educ.* **74**, 129 (1997).
39. Zhi, J., Zhao, S., Zhou, M., Wang, R. & Huang, F. A zinc-conducting chalcogenide electrolyte. *Sci. Adv.* **9**, eade2217 (2023).
40. Wang, S. *et al.* Local lattice softening in semiconductor quantum dots for efficient white light-emitting diodes. *Nat. Photonics* **19**, 952–959 (2025).
41. Yang, Y. *et al.* Entropic ligands for nanocrystals: from unexpected solution properties to outstanding processability. *Nano Lett.* **16**, 2133–2138 (2016).
42. Gwak, N. *et al.* Highly Luminescent Shell-Less Indium Phosphide Quantum Dots Enabled by Atomistically Tailored Surface States. *Adv. Mater.* **36**, 2404480 (2024).
43. Xu, H. *et al.* Dipole–dipole-interaction-assisted self-assembly of quantum dots for highly efficient light-emitting diodes. *Nat. Photon.* **18**, 186–191 (2024).

44. Jang, K. Y. *et al.* Efficient Deep-Blue Light-Emitting Diodes Through Decoupling of Colloidal Perovskite Quantum Dots. *Adv. Mater.* **36**, 2404856 (2024).
45. Lin, X. *et al.* Blue lasers using low-toxicity colloidal quantum dots. *Nat. Nanotechnol.* **20**, 229–236 (2025).
46. Brennan, K. Theory of high-field electronic transport in bulk ZnS and ZnSe. *J. Appl. Phys.* **64**, 4024–4030 (1988).
47. Park, K., Deutsch, Z., Li, J. J., Oron, D. & Weiss, S. Single molecule quantum-confined stark effect measurements of semiconductor nanoparticles at room temperature. *ACS Nano* **6**, 10013–10023 (2012).
48. Hutter, J. *et al*. cp2k: atomistic simulations of condensed matter systems. *WIREs: Comput. Mol. Sci.* **4**, 15–25 (2014).
49. VandeVondele, J. *et al.* Quickstep: Fast and accurate density functional calculations using a mixed Gaussian and plane waves approach. *Comput. Phys. Commun.* **167**, 103–128 (2005).
50. Goedecker, S. *et al*. Separable dual-space Gaussian pseudopotentials. *Phys. Rev. B* **54**, 1703–1710 (1996).
51. Perdew, J. P. *et al*. Generalized gradient approximation made simple. *Phys. Rev. Lett.* **77**, 3865–3868 (1996).
52. Grimme, S. *et al*. A consistent and accurate ab initio parametrization of density functional dispersion correction (DFT-D) for the 94 elements H-Pu. *J. Chem. Phys.* **132**, 154104 (2010).

Figures

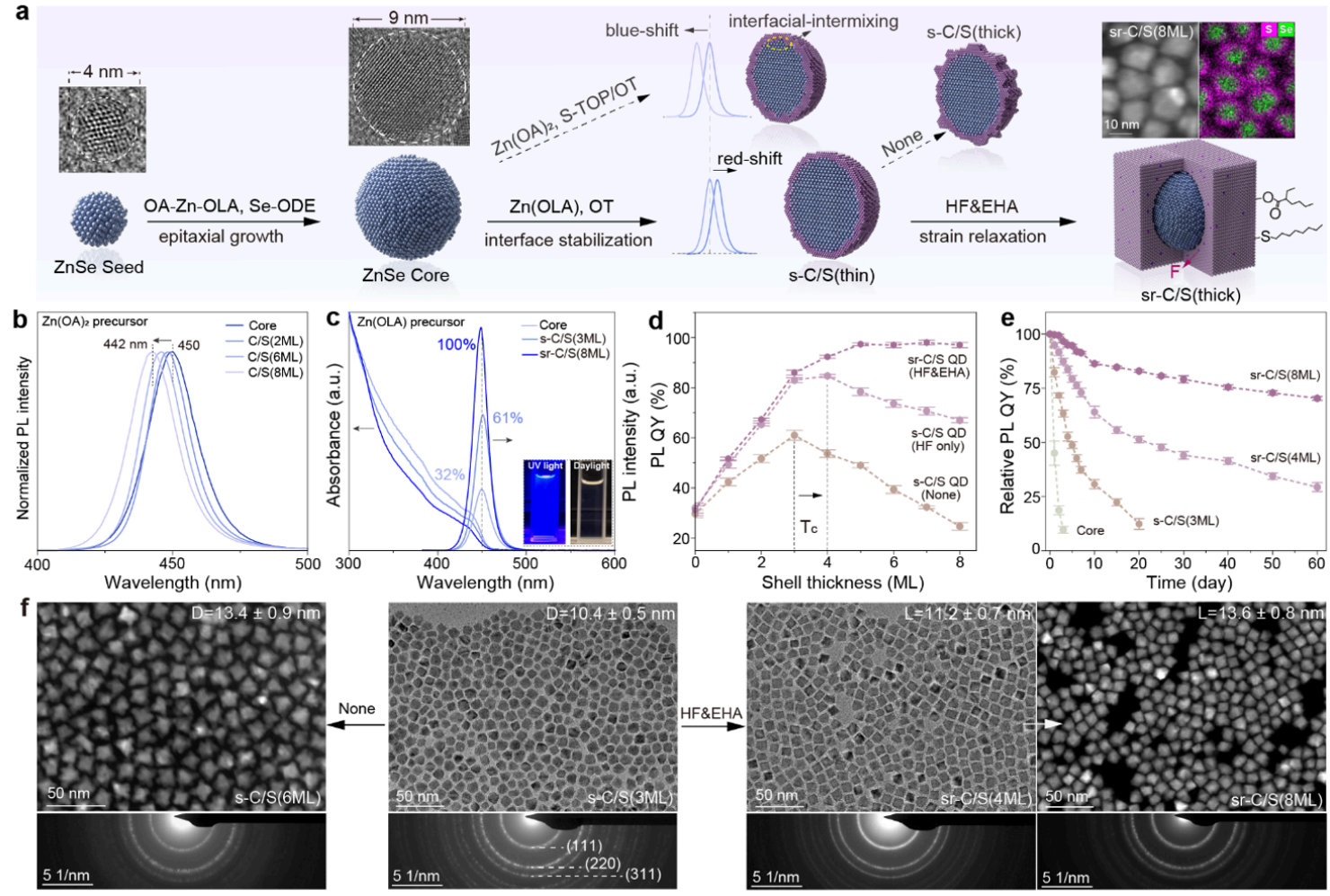


Figure 1

Synthesis and characterization of strain-released thick-shell ZnSe/ZnS QDs. a, Schematic illustration of the synthesis of large ZnSe core, interfacial-intermixed ZnSe/ZnS (C/S), strained ZnSe/ZnS (s-C/S) and strain-released ZnSe/ZnS:F (sr-C/S) QDs, with corresponding atomic scale TEM images and STEM-EDS mapping images. **b**, Evolution of PL spectra of the C/S QDs with different shell thickness by using low-reactivity $Zn(OA)_2$ as shell precursor; e.g., C/S(2ML) denotes ZnSe/ZnS QD with shell thickness of 2 atomic monolayers (ML). **c**, UV-vis absorption and PL spectra of C/S QDs obtained from high-reactivity Zn(OLA) precursor. Inset: photographs of sr-C/S(8ML) QDs in hexane under daylight and 365 nm UV light illumination. **d**, Dependence of PL QYs of C/S QDs on shell thickness under different shell growth conditions. **e**, Evolution of PL QYs of indicated QD-solution over storage time under ambient conditions (temperature: 20 °C, humidity: 65%). **f**, TEM images (top) and the corresponding SAED patterns (bottom) of the indicated C/S QDs obtained from strained and strain-released shell growth stages. “D” is the diameter of QD, and “L” is the length of the side of cube-shaped QD.

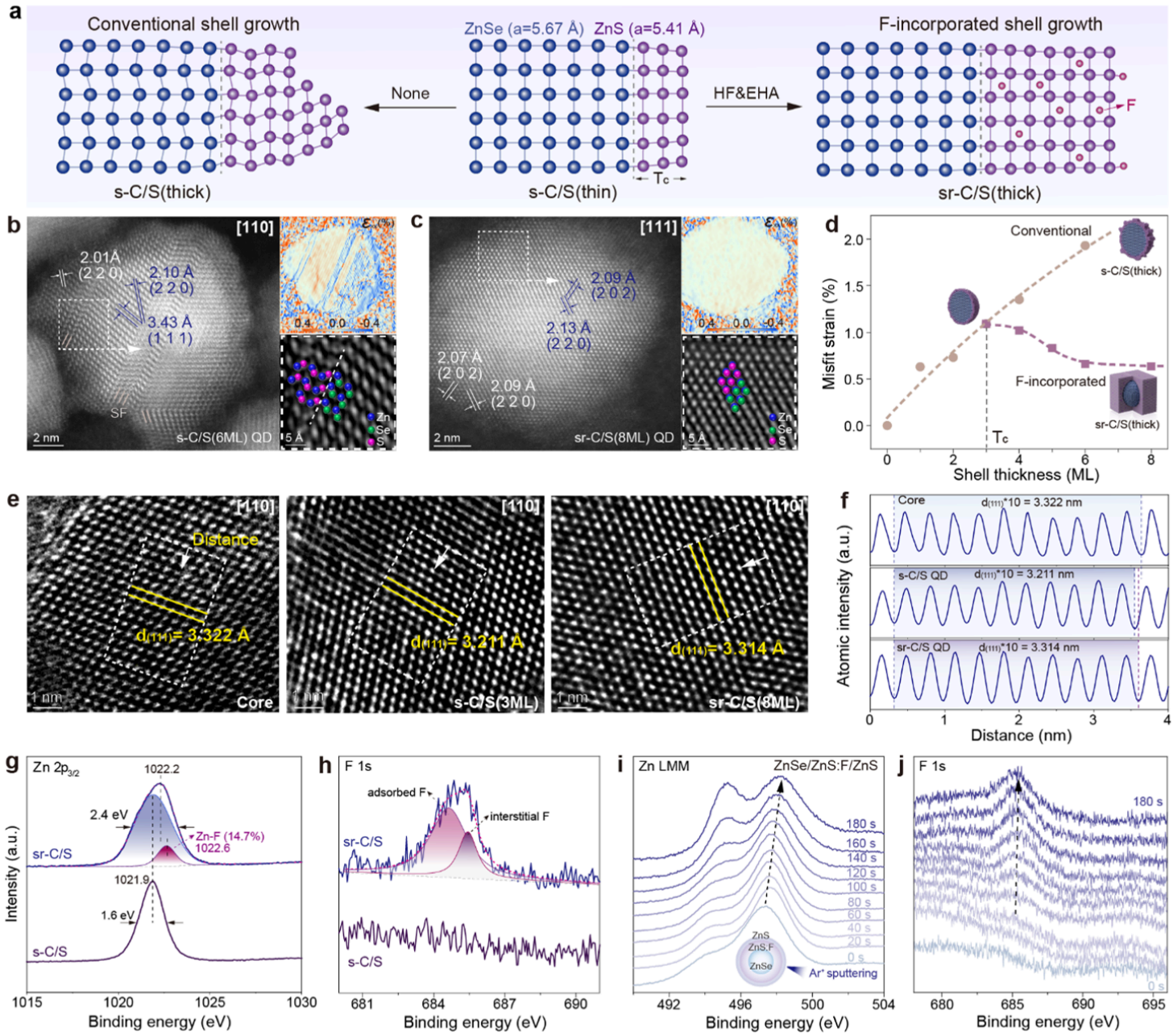


Figure 2

F-incorporated strain-released shell growth. a, Schematic depiction of the formation of irregular shell morphologies due to the strain-induced dislocation lattice defects with shell growth, and the strain-releasing process with shell growth through the F-incorporated shell growth strategy. **b**, Aberration corrected HR-STEM image, geometric phase analysis (GPA) image (top) and inverse FFT filtered image within the dashed areas (bottom) of thick-shell s-C/S QD. **c**, HR-STEM image of sr-C/S QD. **d**, The variation of misfit strain in ZnSe core with outer shell thickness. **e**, Atomic scale TEM images ZnSe core, s-C/S QD, and sr-C/S QD. **f**, The corresponding atomic intensity profiles along the (110) planes in indicated orientation. **g**, XPS spectra of Zn $2p_{3/2}$ for the indicated C/S QDs. **h**, XPS spectra of F 1s for the indicated C/S QDs. **i**, XPS depth profiles of Zn Auger LMM for the double-shelled strain-released ZnSe/ZnS:F/ZnS QDs. **j**, XPS depth profiles of F 1s for ZnSe/ZnS:F/ZnS QDs.

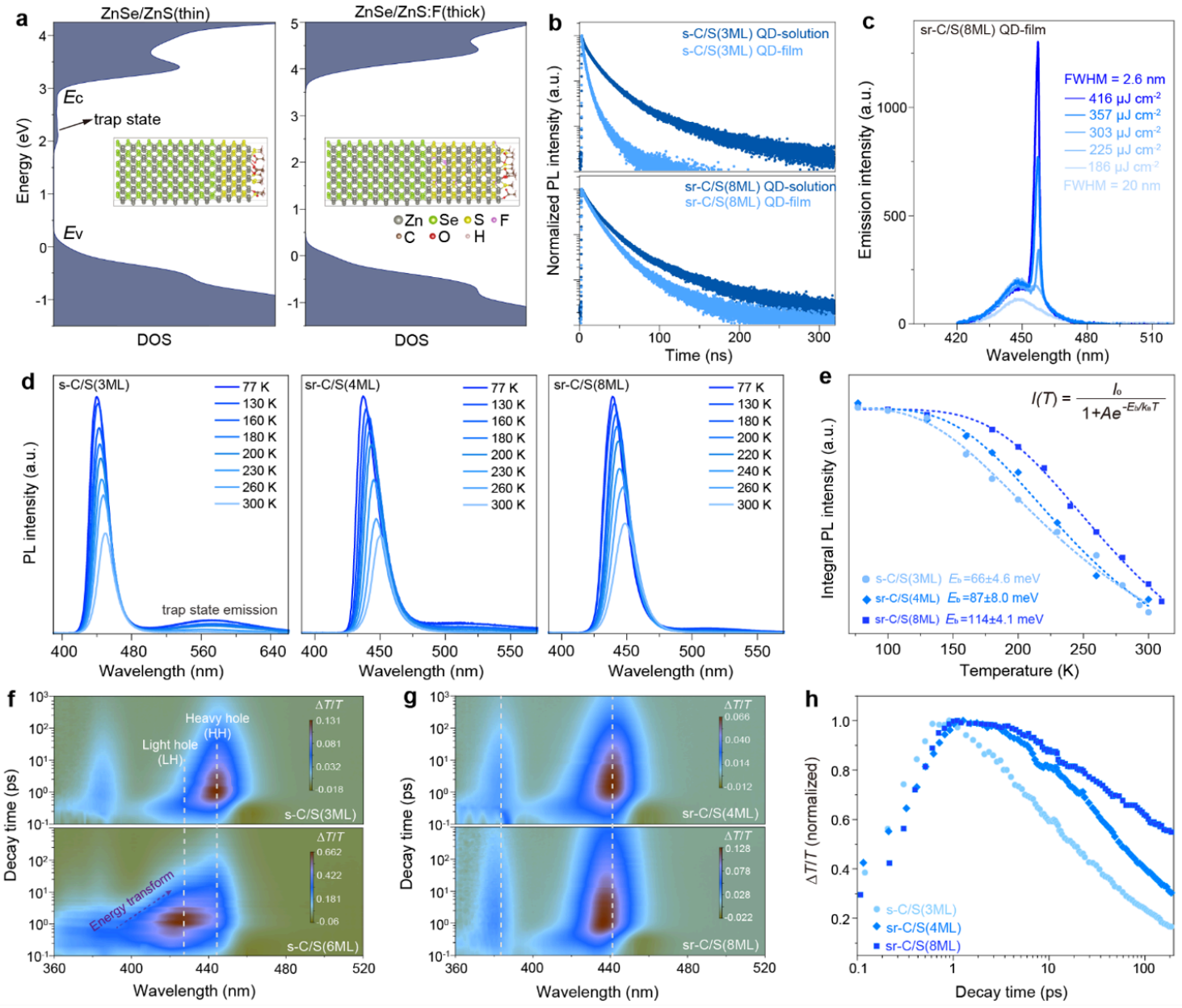


Figure 3

Eliminated mid-gap trap states with thick coherent ZnS shell. a, Calculated density of states (DOS) of the ZnSe/ZnS(thin) and ZnSe/ZnS:F(thick) heterojunctions. *E*v: valence band maximum, *E*c: conduction band minimum. Insets: atomic crystal structures of the indicated heterojunction crystal cells with partial surface ligands bonding with the ZnS surface. **b**, Transient PL decay curves of the s-C/S(3ML) and sr-C/S(8ML) QDs in solution and film states, respectively, measured at a wavelength of 450 nm. **c**, Pump intensity-dependent PL spectra of sr-C/S(8ML) QD film, with strong amplified spontaneous emission (ASE) observed under a power of around 303 μJ cm^{-2}. **d**, Temperature-dependent PL spectra of s-C/S(3ML), sr-C/S(4ML) and sr-C/S(8ML) QDs measured at a range of 77–300 K. **e**, Plots of integrated PL intensity against temperature and fitted with Arrhenius equation. **f**, Two-dimensional maps of transient absorption (TA) spectra of s-C/S QDs with shell thickness of 3 MLs (top) and 6 MLs (bottom). **g**, TA spectra of sr-C/S QDs with shell thickness of 4 MLs (top) and 8 MLs (bottom), acquired under a 350 nm

pump with a fluence of 2.5 μJ cm^{-2}. **h**, Normalized kinetics of ground-state bleaches of s-C/S(3ML), sr-C/S(4ML) and sr-C/S(8ML) QDs with a monitored wavelength of 440 nm.

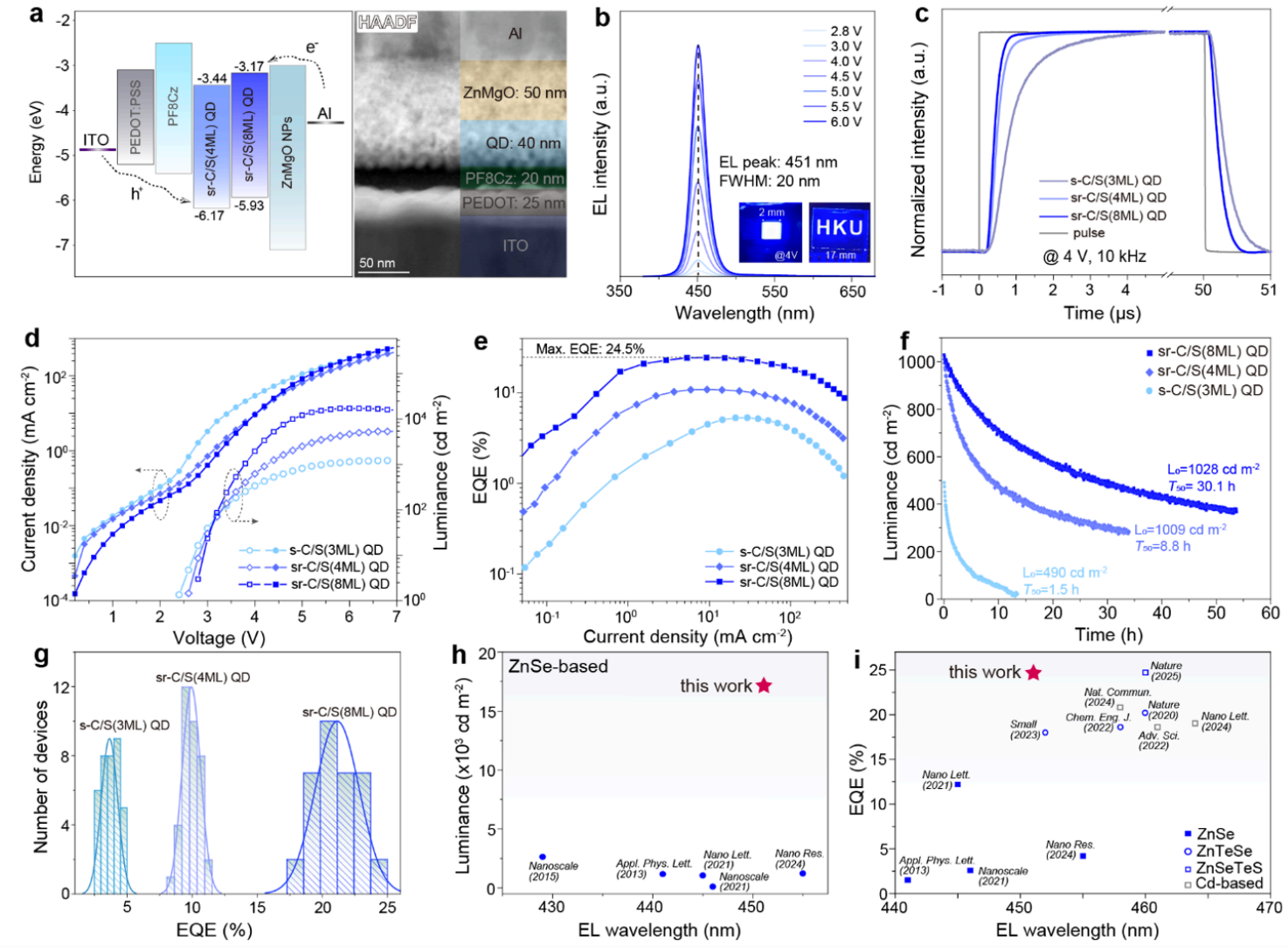


Figure 4

Performance of QLEDs based on ZnSe QDs. a, Energy-band diagram of the QLEDs and the cross-sectional TEM image of the device fabricated with sr-C/S(8ML) QDs. **b**, Voltage-dependent electroluminescence spectra of QLEDs with sr-C/S(8ML) QDs. Inset: photographs of the operating devices. **c**, Transient EL spectra for the QLEDs with indicated QDs under 4 V. **d**, Voltage-dependent current density (left axis) and luminance (right axis). **e**, Current density dependence of the EQEs. **f**, Operational lifetimes for QLEDs with s-C/S(3ML), sr-C/S(4ML), and sr-C/S(8ML) QDs. **g**, EQE histograms of QLEDs fabricated with indicated C/S QDs. **h**, Reported maximum luminance versus EL wavelength of the ZnSe-based QLEDs. **i**, Reported peak EQE versus EL wavelength of representative blue-emitting QLEDs.

Supplementary Files

This is a list of supplementary files associated with this preprint. Click to download.

- SupplementaryInformation.docx